

Alluvial morphodynamics of low-slope bedrock reaches transporting non-uniform bed material

Sadegh Jafarinik¹ and Enrica Viparelli¹

¹University of South Carolina

November 24, 2022

Abstract

Research on bedrock rivers primarily focused on bedrock incision and, to the best of our knowledge, morphodynamic models have not yet considered the variability of sediment grain size and the presence of small scale bedforms in low-slope (slope < 0.005) bedrock reaches. Further, very few models can quantify spatial and temporal changes in the fraction of channel bed covered with alluvium (alluvial cover) within these reaches. Here we present a novel formulation of alluvial morphodynamics of low-slope bedrock reaches transporting non-uniform bed material. The formulation is implemented in a one-dimensional model and validated against laboratory experiments on bedrock reaches downstream of stable alluvial-bedrock transitions, where the flow accelerates in space. The validated model is used to study the alluvial morphodynamics of bedrock reaches upstream of stable bedrock-alluvial transitions. Equilibrium results show that the interactions between flow, sediment transport and non-erodible bedrock surface result in a flow decelerating in the streamwise direction. The effects of this spatial flow deceleration are 1) a streamwise increase in alluvial cover, and 2) the formation of a pattern of downstream coarsening of bed surface sediment. We then investigated the effects of sea level rise/fall on the location of alluvial-bedrock and bedrock-alluvial transitions. In the case of sea level rise, alluvial-bedrock transitions migrate downstream and bedrock-alluvial transitions migrate upstream. Opposite migration directions are expected in the case of sea level fall.

1 **Alluvial morphodynamics of low-slope bedrock reaches transporting non-uniform**
2 **bed material**

3
4
5
6
7
8
9
10
11
12 **S. Jafarinik¹, and E. Viparelli¹**

13 ¹Civil and Environmental Engineering Department, University of South Carolina, Columbia,
14 South Carolina, USA

15
16 Corresponding author: Enrica Viparelli (viparell@cec.sc.edu)

17
18
19
20
21
22
23
24 **Key Points (at the end):**

- 25 • We developed, implemented and tested a novel formulation for alluvial morphodynamics
26 of bedrock reaches transporting non-uniform bed material
- 27 • Stable patterns of downstream coarsening are predicted upstream of a stable bedrock-
28 alluvial transition
- 29 • In presence of sea level rise, a bedrock-alluvial transition migrates upstream and an
30 alluvial-bedrock transition migrates downstream. The opposite is expected in case of sea
31 level fall.
32

33 **Abstract**

34 Research on bedrock rivers primarily focused on bedrock incision and, to the best of our
35 knowledge, morphodynamic models have not yet considered the variability of sediment grain
36 size and the presence of small scale bedforms in low-slope (slope < 0.005) bedrock reaches.
37 Further, very few models can quantify spatial and temporal changes in the fraction of channel
38 bed covered with alluvium (alluvial cover) within these reaches. Here we present a novel
39 formulation of alluvial morphodynamics of low-slope bedrock reaches transporting non-uniform
40 bed material. The formulation is implemented in a one-dimensional model and validated against
41 laboratory experiments on bedrock reaches downstream of stable alluvial-bedrock transitions,
42 where the flow accelerates in space. The validated model is used to study the alluvial
43 morphodynamics of bedrock reaches upstream of stable bedrock-alluvial transitions.
44 Equilibrium results show that the interactions between flow, sediment transport and non-erodible
45 bedrock surface result in a flow decelerating in the streamwise direction. The effects of this
46 spatial flow deceleration are 1) a streamwise increase in alluvial cover, and 2) the formation of a
47 pattern of downstream coarsening of bed surface sediment. We then investigated the effects of
48 sea level rise/fall on the location of alluvial-bedrock and bedrock-alluvial transitions. In the case
49 of sea level rise, alluvial-bedrock transitions migrate downstream and bedrock-alluvial
50 transitions migrate upstream. Opposite migration directions are expected in the case of sea level
51 fall.

52

53

54

55

56 **1 Introduction**

57 Bedrock reaches are frequently found in upland areas where the bed material is relatively
58 coarse, is preferentially transported as bedload, and small scale bedforms such as dunes are
59 absent [Whipple *et al.*, 2000; Whipple and Tucker, 2002; Whipple, 2004; Sklar and Dietrich,
60 2004; Turowski *et al.*, 2007; Gasparini *et al.*, 2007; Chatanantavet and Parker, 2008, 2009;
61 Lamb *et al.*, 2008; Lague, 2010, 2014; Hodge *et al.*, 2011, 2016; Chatanantavet *et al.*, 2013;
62 Johnson, 2014; Zhang *et al.*, 2015; Inoue *et al.*, 2014]. Recent field studies, however, show that
63 bedrock reaches can also be found in lowland areas, where the bed material is relatively fine and
64 small scale bedforms, such as dunes, are present. These reaches can be bounded by an upstream
65 alluvial-bedrock transition and may also present a downstream bedrock-alluvial transition
66 [Nittrouer *et al.*, 2011; Shaw *et al.*, 2013; Shaw and Mohrig, 2014].

67 *Viparelli et al.* [2015] demonstrated that low-slope bedrock rivers, i.e. rivers with
68 bedrock and alluvial slopes milder than 0.005 [Chatanantavet and Parker, 2008], can reach an
69 equilibrium configuration in the absence of bedrock incision, sea level rise and subsidence. At
70 equilibrium, the location of alluvial-bedrock and bedrock-alluvial transitions does not change in
71 space and in time [Viparelli *et al.*, 2015].

72 Equilibrium is a condition in which bed elevation averaged over time scales that are long
73 compared to the time scales of bedform migration [Blom *et al.*, 2006] and bedload transport
74 [Wong *et al.*, 2007] is constant in time [Anderson *et al.*, 1975]. If base level, formative discharge
75 and sediment supply are constant in time, in equilibrium alluvial reaches the bed material load is
76 everywhere equal to the sediment supply and to the transport capacity of the flow, [Parker,
77 2004]. If abrasion is not accounted for, equilibrium grain size distributions of bed material load
78 and of bed surface sediment do not change in space and time [Blom *et al.*, 2016]. In particular,

79 the grain size distribution of the bed material load is equal to the grain size distribution of the
80 sediment supply, and the grain size distribution of the bed surface sediment is generally coarser
81 than the grain size distribution of the sediment supply to regulate the different mobility of coarse
82 and fine grains [*Blom et al.*, 2016 and references therein].

83 In low-slope bedrock channels transporting sand as bed material, equilibrium is
84 characterized by steady and not uniform flow conditions. Spatial changes in mean flow velocity
85 are associated with spatial changes in alluvial cover, i.e. the areal fraction of bed surface covered
86 with alluvium [*Viparelli et al.*, 2015]. In particular, in case of flow acceleration (e.g. downstream
87 of a stable alluvial-bedrock transition) the alluvial cover decreases in the streamwise direction,
88 and the opposite is observed in the case of spatial flow deceleration (e.g. upstream of a stable
89 bedrock-alluvial transition) [*Viparelli et al.*, 2015]. The conservation of channel bed material
90 imposes that at equilibrium the bed material load is equal to the sediment supply. In equilibrium
91 bedrock rivers, spatial changes of bed material transport capacity are balanced by streamwise
92 changes in alluvial cover, which limit sediment availability so that the bed material load is
93 everywhere equal to the sediment supply [*Viparelli et al.*, 2015].

94 Laboratory experiments on equilibrium low-slope bedrock rivers transporting non-
95 uniform sand showed that, as the flow spatially accelerates downstream of a stable alluvial-
96 bedrock transition, flow resistances decrease in the streamwise direction due to downstream
97 fining of the bed surface sediment (reduction of skin friction), streamwise decrease in bedform
98 height (reduction of form drag), or a combination of the two [*Jafarinik et al.*, 2019]. Thus, in
99 response to flow acceleration/deceleration 1) spatial variations in bedform height and wavelength
100 may result in a spatially changing form drag, and 2) stable patterns of downstream fining or
101 coarsening of bed surface sediment may form [*Jafarinik et al.*, 2019].

102 To the best of our knowledge, models of alluvial morphodynamics of bedrock rivers do
103 not account for the non-uniformity of the bed material grain size and for changes in flow
104 resistances associated with a spatial change in the bedform geometry and grain size distribution
105 of the bed surface sediment [*Lague, 2010; Zhang et al., 2015; Johnson, 2014; Viparelli et al.,*
106 *2015*]. Here we present a novel formulation for the alluvial morphodynamics of bedrock rivers
107 that accounts for the non-uniformity of the bed material grain size and the presence of small
108 scale bedforms. We implemented the formulation in a one-dimensional model and validate the
109 model against experimental results [*Jafarinik et al., 2019*]. We apply the validated model to
110 study equilibrium of a low-slope bedrock reach with a stable bedrock-alluvial transition, and the
111 morphodynamics of a bedrock reach with variable downstream water level. Model applicability
112 to steep bedrock rivers (bedrock slope greater than 0.005), where equilibrium conditions may be
113 initial-condition dependent [*Chatanantavet and Parker, 2008*], is also briefly discussed.

114

115 **2 Model formulation**

116 The model formulation is not site specific and can be applied to either field or laboratory
117 scales. Application-specific relations to compute flow resistances and bed material transport
118 capacity should be chosen based on problem characteristics. Model governing equations are the
119 one-dimensional shallow water equations of mass and momentum conservation for open channel
120 flow, the grain size specific equation of conservation of bed material, and the equation of
121 conservation of total (summed over all the grain sizes) bed material.

122 The following assumptions and approximations are introduced to simplify the problem:

- 123 1. The ratio between the volumetric bed material load and the flow discharge is assumed to
124 be orders of magnitude smaller than one, so that the quasi-steady approximation holds for the
125 flow [*De Vries*, 1965];
- 126 2. The bedrock is assumed to be non-erodible. The extension of the formulation to erodible
127 bedrock surfaces is relatively straightforward [e.g. *Sklar and Dietrich*, 2004; *Lamb et al.*, 2008];
- 128 3. A procedure to account for different roughness between the smooth sidewalls and the
129 rough bed is implemented for lab scale applications [*Vanoni and Brooks*, 1957];
- 130 4. When applied at field scale, the model describes the long-term evolution of the river
131 channel. It does not account for the exchange of sediment between the channel and the floodplain
132 due to for example overbank deposition of suspended sediment, channel migration or widening
133 [e.g. *Viparelli et al.*, 2011; *Lauer et al.*, 2016];
- 134 5. Base level is assumed constant, but the modification of the formulation to account for
135 subsidence, uplift or sea level rise is straightforward, as shown in the discussion section of this
136 manuscript;
- 137 6. The bed material is preferentially transported as bedload. The implementation of grain
138 size specific suspended load calculations is also relatively simple;
- 139 7. The cross section is assumed to be rectangular with uniform width that does not change
140 in time. The extension to the case of a spatially varying cross section with geometry that does
141 not change in time is cumbersome but not complex [*Viparelli et al.*, 2015]; and
- 142 8. The active layer approximation is used to model the exchange of bed material between
143 the mobile bed and the bedload [*Hirano*, 1971; *Parker*, 1991a, b]

144 2.1 Model geometry

145 The schematic longitudinal profile of the modeled system is presented in Figure 1, where
146 the black line represents the deepest portion of the bedrock surface with elevation η_b , and slope
147 S_b [Zhang *et al.*, 2015], the grey line denotes the locally averaged elevation of the alluvial bed η
148 [Parker *et al.*, 2000; Zhang *et al.*, 2015] and ζ is the downstream water surface elevation. The
149 dashed line at elevation $\eta_b + L_{ac}$ identifies the minimum elevation of the alluvial bed such that in-
150 channel sediment transport processes are not affected by the underlying bedrock [Viparelli *et al.*,
151 2015]. In other words, L_{ac} represents the minimum thickness of alluvial cover for complete
152 channel bed alluviation. In a bedrock reach the elevation of the alluvial bed, η , is smaller than
153 $\eta_b + L_{ac}$, in an alluvial reach $\eta > \eta_b + L_{ac}$, $\eta = \eta_b + L_{ac}$ corresponds to the location of a bedrock-
154 alluvial or an alluvial-bedrock transition [Viparelli *et al.*, 2015].

155

156 2.2 Flow equations

157 The one-dimensional shallow water equations of mass and momentum conservation for
158 open channel flow are presented in equations (1) and (2) [Chaudhry, 2007].

$$\frac{\partial H}{\partial t} + \frac{\partial UH}{\partial x} = 0 \quad (1)$$

$$\frac{\partial U}{\partial t} + g \frac{\partial}{\partial x} \left(\frac{U^2}{2g} + H \right) = g(S - S_f) \quad (2)$$

159 where x and t respectively represent streamwise and temporal coordinates, U and H respectively
160 denote the flow depth and the mean flow velocity, g is the acceleration of gravity, S is the
161 channel bed slope defined herein as the slope of the alluvial bed $S = -\partial\eta/\partial x$, and S_f denotes the
162 friction slope. Equations (1) and (2) are simplified with the quasi-steady approximation [De
163 Vries, 1965], i.e. time derivatives are dropped and equations (1) and (2) reduce to

$$q_w = UH \quad (3)$$

$$g \frac{\partial}{\partial x} \left(\frac{U^2}{2g} + H \right) = g(S_o - S_f) \quad (4)$$

164 where q_w is the flow discharge per unit channel width. Substituting equation (3) into equation
 165 (4), the backwater equation for one-dimensional gradually varied steady flow is obtained

$$\frac{\partial H}{\partial x} = \frac{S - S_f}{1 - Fr^2} \quad (5)$$

166 where Fr is the Froude number defined as U/\sqrt{gH} and S_f represents the friction slope which is
 167 defined as

$$S_f = \frac{C_f U^2}{gR_h} \quad (6)$$

168 where C_f is a non-dimensional friction coefficient and R_h is the hydraulic radius. The general
 169 friction coefficient formulation used herein is the Manning-Strickler formulation as follows.

$$C_f^{-1/2} = \alpha_r \left(\frac{R_h}{k} \right)^{1/6} \quad (7)$$

170 where α_r is a model parameter equal to 8.1 [Parker, 2004] and k denotes the roughness height.
 171 The calculation of C_f depends on the problem of interest.

172 Equation (5) is integrated with a first order, finite difference scheme in the upstream
 173 direction with downstream boundary condition expressed in terms of known downstream water
 174 level, as appropriate in the case of subcritical flows.

175

176 2.3 Conservation of bed material

177 To account for the non-uniformity of the bed material grain size, sediment fluxes between
 178 the alluvial bed and the bed material load are modeled with the aid of the active layer

179 approximation. In active layer-based models, the deposit is divided in two regions, the active
180 layer and the substrate. The active layer represents the topmost part of the deposit that interacts
181 with the bed material load. The substrate is the part of the deposit underneath the active layer
182 with grain size distribution that can change in space, i.e. in the vertical and streamwise direction
183 [Parker et al., 2000].

184 The definition of the active layer thickness L_a is not straightforward and relies on
185 observations. In gravel bed rivers, where small scale bedforms such as dunes are generally
186 absent [Parker and Klingemann, 1982], the active layer thickness scales with the coarsest grain
187 sizes of the bed surface material. In sand bed rivers, where small scale bedforms such as dunes
188 are generally present, the thickness of the active layer is hard to define and it generally scales
189 with bedform height [Blom, 2008].

190 In active layer-based models, two equations of conservation of bed material are solved: 1)
191 the equation of conservation of total, i.e., summed over all the grain sizes, bed material to
192 compute the changes in mean bed elevation, and 2) the grain size specific equation of
193 conservation of bed material to compute spatiotemporal changes of active layer sediment size
194 distribution. In the continuing of this section we illustrate how equations of conservation of
195 alluvial bed material can be used to model the alluvial morphodynamics of bedrock rivers.

196

197 *i. Equation of conservation of bed material summed over all the grain sizes*

198 The equation of conservation of total bed material in bedrock reaches takes the form
199 [Zhang et al., 2015]

$$(1 - \lambda_p)p_c \frac{\partial \eta}{\partial t} = -\frac{\partial q_{bT}}{\partial x} \quad (8)$$

200 where λ_p denotes the bulk porosity of the alluvial deposit, q_{bT} is the total volumetric bed material
 201 load per unit channel width and p_c represents the alluvial cover defined as the areal fraction of
 202 bed that is covered with alluvium [Nelson and Seminara, 2012; Inoue et al. 2014 and Johnson,
 203 2014]. The total volumetric bed material load per unit channel width is equal to the total
 204 volumetric bed material transport capacity q_{bTc} computed with an empirical relation such as
 205 Ashida and Michiue [1972] or Wilcock and Crowe [2003] multiplied by p_c [Sklar and Dietrich,
 206 2004].

207

208 ii. *Grain size specific equation of conservation of bed material*

209 If the density of the bed material does not vary from one characteristic grain size to the
 210 other, the one-dimensional, grain size specific conservation of bed material can be phrased as
 211 follows: the time rate of change of bed material with characteristic grain size D_i in a control
 212 volume is equal to the net influx of bed material with grain size D_i . In bedload dominated rivers,
 213 the grain size specific equation of conservation of bed material takes the following form (see
 214 Zhang et al. [2015] for the derivation in the case of uniform sediment)

$$(1 - \lambda_p) \frac{\partial}{\partial t} \int_{\eta_b}^{\eta} p_b f_i dz = -\frac{\partial q_{bi}}{\partial x} \quad (9)$$

215 where z denotes an upward oriented vertical coordinate, p_b represents the probability that a point
 216 at elevation z relative to an arbitrary datum is not bedrock [Zhang et al., 2015], f_i is the volume
 217 fraction content of bed material with characteristic grain size D_i at elevation z and q_{bi} is the
 218 bedload transport rate of bed material particles with characteristic grain size D_i . In general, f_i

219 varies in space (x and z) and in time. In a fully alluvial system, the lower limit of integration in
 220 equation (12) refers to a point very deep in the alluvial deposit [*Parker et al.*, 2000]. Here, as in
 221 *Zhang et al.* [2015], the lower limit of integration η_b corresponds to the elevation of the *bottom*
 222 *of the bedrock surface*, i.e. a point where $p_b = 0.05$. The grain size specific bedload transport
 223 rate, q_{bi} is equal to the product of the grain size specific bedload transport capacity q_{bic} and p_c .
 224 The sum of q_{bi} over all the grain size fractions is equal to q_{bT} .

225 The active layer approximation [*Hirano*, 1971; *Parker*, 1991a, b] is used to solve the
 226 integral on the left-hand side of equation (9). The alluvial deposit is thus divided in two parts,
 227 the active layer and the substrate. The active layer is a relatively thin, mixed layer on the
 228 topmost part of the deposit whose sediment size distribution can change in time due to the
 229 exchange of sediment with the bedload transport. The substrate is the deposit between the
 230 bedrock surface and the active layer. Substrate sediment size distribution can change in x and z
 231 but not in time, unless η changes in time. In other words, the volume fraction content of
 232 sediment with characteristic grain size D_i in the active layer F_i can change in the streamwise
 233 direction and in time, and the volume fraction content of substrate sediment in the generic grain
 234 size range f_i changes in time when the channel bed aggrades or degrades.

235 If the active layer-substrate interface elevation is higher than the elevation of the bottom
 236 of the bedrock surface, $(\eta - L_a) \geq \eta_b$, we express the left hand side of equation (9) as the sum of
 237 the integral of $p_b f_i$ in the substrate (between η_b and $\eta - L_a$) and in the active layer (between $\eta - L_a$
 238 and η) with L_a denoting the active layer thickness in the case of a fully alluvial system, equation
 239 (10a). If the active layer-substrate interface elevation is below the bottom of the bedrock
 240 surface, $(\eta - L_a) < \eta_b$, the left-hand side of equation (9) is equal to the integral of $p_b f_i$ between η_b
 241 and η , equation (10b). The integral of equation (9) thus takes the form

$$\frac{\partial}{\partial t} \int_{\eta_b}^{\eta} p_b f_i dz = \frac{\partial}{\partial t} \left(\int_{\eta_b}^{\eta-L_a} p_b f_i' dz + \int_{\eta-L_a}^{\eta} p_b F_i dz \right) \quad \text{if } (\eta - L_a) \geq \eta_b \quad (10a)$$

$$\frac{\partial}{\partial t} \int_{\eta_b}^{\eta} p_b f_i dz = \frac{\partial}{\partial t} \int_{\eta_b}^{\eta} p_b F_i dz \quad \text{if } (\eta - L_a) < \eta_b \quad (10b)$$

)

242 In the absence of bedrock incision, subsidence and uplift, the limits of integration that are
 243 a function of time are η and $\eta - L_a$. The Leibnitz rule is thus applied to compute the derivative of
 244 the first integral on the right-hand side of equation (10a) as

$$\frac{\partial}{\partial t} \int_{\eta_b}^{\eta-L_a} p_b f_i' dz = \int_{\eta_b}^{\eta-L_a} \frac{\partial(p_b f_i')}{\partial t} dz + (p_b f_i')|_{z=\eta-L_a} \frac{\partial}{\partial t} (\eta - L_a) = p_{bl} f_{li} \frac{\partial}{\partial t} (\eta - L_a) \quad (11)$$

245 where f_{li} denotes the volume fraction content of bed material with grain size D_i at the active
 246 layer-substrate interface and p_{bl} is probability that a point at the active layer-substrate interface (z
 247 $= \eta - L_a$) is either in water or in alluvium.

248 The derivative of the second integral on the right-hand side of equations (10a) and (10b)
 249 is easy to compute because the active layer is a mixed layer (F_i does not vary in the z direction).
 250 Further, recalling that η is the locally averaged elevation of the alluvium, the integral of p_b
 251 between $(\eta - L_a)$ and η represents the volume of sediment per unit bed area in the active layer,
 252 i.e., the average thickness of the active layer, $L_{a,av}$ in the bedrock reach. For the same reason, the
 253 integral in equation (13b) is equal to $F_i L_{a,av}$.

254 In an alluvial system $p_b = 1$, $L_{a,av} = L_a$ and the volume of active layer sediment per unit
 255 bed area with grain size D_i is equal to $F_i L_a$. In bedrock reaches, $L_{a,av} < L_a$ due to the presence of
 256 exposed bedrock. Substituting equations (10) and (11) in equations (9), the grain size specific
 257 equation of conservation of bed material takes the form

$$(1 - \lambda_p) \left[p_{bl} f_{li} \frac{\partial}{\partial t} (\eta - L_a) + \frac{\partial}{\partial t} (F_i L_{a,av}) \right] = - \frac{\partial q_{bi}}{\partial x} \quad (12)$$

258 When $(\eta - L_a) < \eta_b$, the probability that a point at elevation $(\eta - L_a)$ is either in water or in
 259 alluvium, p_{bl} , is equal to zero and consequently the sediment flux between the active layer and
 260 the substrate, i.e. the first term in the left-hand side of equation (12), is also equal to zero.

261 When $(\eta - L_a) \geq \eta_b$, the volume fraction content of bed material at the active layer-
 262 substrate interface, f_{li} , is computed with the *Hoey and Ferguson* [1994] formulation, as

$$f_{li} = \begin{cases} f'_i |_{z=\eta-L_a}, & \frac{\partial \eta}{\partial t} < 0 \\ \alpha F_i + (1 - \alpha) f_{load,i}, & \frac{\partial \eta}{\partial t} \geq 0 \end{cases} \quad (13)$$

263 where $0 < \alpha < 1$ and $f_{load,i}$ is the volume fraction content of bed material with characteristic grain
 264 size D_i in bedload transport q_{bi}/q_{bT} . To determine p_{bl} , i.e. the probability that a point at elevation
 265 $(\eta - L_a)$ is in alluvium or water, we follow *Zhang et al.* [2015] and *Viparelli et al.* [2015]:

266 1) we characterize the local variation in bedrock elevation in terms of a minimum thickness
 267 of alluvial cover for complete channel bed alluviation L_{ac} . In other words, L_{ac} represents
 268 the minimum vertical distance between the top of the alluvium and the bottom of the
 269 bedrock surface such that in-channel sediment transport processes are not influenced by
 270 the bedrock surface (see Figure 1) [*Viparelli et al.*, 2015];

271 2) we recall that $(\eta - \eta_b)$ represents the elevation difference between the locally averaged top
 272 of alluvium and the bottom of the bedrock surface and that $[1 - p_b(z)]$ represents the
 273 probability that a point at elevation z is bedrock [*Zhang et al.*, 2015]. Changes in bed
 274 level due to bedload transport and bedform migration [*Parker et al.*, 2000; *Blom et al.*,

275 2003; Wong *et al.*, 2007] are not modeled, thus if $z \leq \eta$, $p_b(z)$ represents the probability
276 that a point at elevation z is in alluvium, and if $z > \eta$, $p_b(z)$ represents the probability that a
277 point at elevation z is in water; consequently

278 3) the cover fraction p_c at elevation z , with $\eta_b < z \leq \eta$ is equal to p_b , i.e. $p_c[(z - \eta_b)/L_{ac}] = p_b(z)$
279 [Zhang *et al.*, 2015].

280

281 2.4 The flow of the calculation

282 The modeled domain is divided into N reaches bounded by $N+1$ computational nodes.
283 Initial conditions are the longitudinal profile of the alluvial bed, the grain size distributions of the
284 active layer and of the substrate. Model boundary conditions are assigned in terms of a
285 longitudinal profile of the bottom of the bedrock surface, flow rate, sediment feed rate and grain
286 size distribution, and downstream water surface elevation. It is important to mention here that in
287 the simulation presented below the grain size distribution of the substrate is assumed to be equal
288 to the grain size distribution of the sediment feed.

289 The flow is assumed to be Froude subcritical and equation (5) is integrated in the
290 upstream direction. Bed shear stresses are estimated in each computational node, and bedload
291 transport rates are computed with a surface-based formulation modified to account for the
292 presence of exposed bedrock [Jafarinik *et al.*, 2019]. The equation of conservation of total bed
293 material (equation 8) is integrated to estimate the time rate of change of mean alluvial bed
294 elevation, and finally the grain size specific equation of conservation of active layer sediment
295 (equation 12) is integrated to update the grain size distribution of active layer sediment.
296 Calculations are either repeated for a user specified duration of simulated time, or until the

297 system reaches equilibrium, i.e. when the alluvial bed elevation does not change in time and the
298 bedload transport rate becomes equal to the upstream sediment supply in each node.

299

300 **3 Overview of the laboratory experiments**

301 The morphodynamic framework presented above is implemented in a one-dimensional
302 model and validated against laboratory experiments on equilibrium mixed bedrock channels
303 downstream of an alluvial-bedrock transition [Jafarinik *et al.*, 2019]. Jafarinik *et al.* [2019]
304 performed four pairs of experiments to compare equilibrium conditions in fully alluvial and
305 mixed bedrock-alluvial reaches subject to the same flow rate and sediment supply. The
306 experiments were performed in a 6 m long and 0.19 m wide sediment feed flume with constant
307 feed rate, flow rate and water surface base level. The model bedrock was a sheet of marine
308 plywood and sand grains were glued to the plywood to create a somewhat rough boundary. The
309 grain size distribution of the sediment types used in the experiments is presented in Figure 2,
310 where the black line is the grain size distribution of the uniform sand with geometric mean
311 diameter $D_g = 1.11$ mm and geometric standard deviation $\sigma_g = 1.44$ mm and the grey line is the
312 grain size distribution of the nonuniform sand with geometric mean diameter $D_g = 0.87$ mm and
313 geometric standard deviation $\sigma_g = 1.69$ mm. At equilibrium, time series of bed and water surface
314 elevation were measured with ultrasonic probes, alluvial cover and flow characteristics averaged
315 over a series of bedforms were computed. Sediment samples were then collected to measure the
316 grain size distribution of the bed surface, defined as the entire thickness of the alluvial layer in
317 the bedrock reaches [Jafarinik *et al.*, 2019].

318 Prior to model verification, which is a necessary step to determine if the morphodynamic
319 formulation presented above is adequate to simulate the alluvial morphodynamics of low-slope

320 bedrock rivers, sub-models to predict alluvial cover [Viparelli et al., 2015], bedform height,
 321 bedload transport rates and flow resistances have to be determined or validated using the
 322 experimental data. If one of these sub-models does not adequately reproduce the experimental
 323 observations, the proposed morphodynamic formulation cannot be verified against the
 324 experimental results because the differences between numerical predictions and experimental
 325 data will be (at least) partially due to the use of an inadequate sub-model [Viparelli et al., 2010].

326

327 3.1 Alluvial cover

328 In the model simulations the alluvial cover is computed with the linear relation used by
 329 Viparelli et al. [2015] which has not been compared with laboratory or field data

$$p_c = \begin{cases} 0.05 + 0.95 \frac{\eta - \eta_b}{L_{ac}} & \text{if } \frac{\eta - \eta_b}{L_{ac}} \leq 1 \\ 1 & \text{if } \frac{\eta - \eta_b}{L_{ac}} > 1 \end{cases} \quad (14)$$

330 Equation (14) is validated against the Jafarinik et al. [2019] experiments. The average
 331 thickness of alluvial cover L_{ac} in the equation is assumed to be equal to $1.5\sigma_a$, with σ_a being the
 332 standard deviation of bed elevation changes over time scales that are short compared to the time
 333 scales of channel bed aggradation/degradation. The subscript a indicates that the standard
 334 deviation of bed elevations is determined in fully alluvial reaches subject to the same flow rate
 335 and sediment supply as the bedrock reach of interest [Jafarinik et al., 2019]. Tuijnder et al.
 336 [2009] performed experiments on sand dunes migrating on an immobile gravel layer and showed
 337 that the interaction between the gravel layer and the bedforms became negligible when the
 338 average thickness of the alluvial layer was equal or greater than ~ 1.5 times the bedform height.

339 The comparison between model predictions and experimental results is presented in
340 Figure 3, where the dots represent the experimental points, the black line is equation (14) and the
341 dashed lines indicate $\pm 25\%$ around the predicted value. The difference between predictions and
342 laboratory measurements is larger than 25% in only 3 cases corresponding to $\sim 10\%$ of the
343 experimental points. Thus, equation (14) reasonably reproduces the experimental observations
344 and can be used to predict the alluvial cover of the *Jafarinik et al.* [2019] experiments in a one-
345 dimensional model of alluvial morphodynamics of bedrock rivers.

346

347 *3.2 Bedform amplitude predictor*

348 The active layer thickness in presence of small scale bedforms generally scales with
349 bedform amplitude [*Blom, 2008*]. In bedrock reaches bedform amplitude is generally smaller
350 than in alluvial reaches subject to the same flow rate and sediment supply [*Tuijnder et al., 2009*;
351 *Jafarinik et al., 2019*]. In addition, bedform amplitude may also change in space as a
352 consequence of the non-uniformity of the flow on the bedrock reach [*Jafarinik et al., 2019*].

353 Predictive relations linking bedform amplitude in a bedrock reach with flow
354 characteristics are, to the best of our knowledge, not available in the literature. Here we use the
355 standard deviation of time series of elevations at equilibrium σ as a measure of bedform
356 amplitude [*Jafarinik et al., 2019*]. To estimate σ we use *Jafarinik et al.* [2019] data and we find
357 a linear regression between the Froude number of the flow and the non-dimensional standard
358 deviation of bed elevations σ/D_{sg} with D_{sg} being the geometric mean size of the bed surface
359 sediment

$$\frac{\sigma}{D_{sg}} = -25.97Fr + 23.5 \quad (15)$$

360 Experimental measurements and equation (15) are presented in Figure 4, where the dots
361 are the experimental points and the line is equation (15). The ratio σ/D_{sg} decreases with
362 increasing Froude number, i.e. the dune height decreases as the flow accelerates in the
363 streamwise direction downstream of a stable alluvial-bedrock transition. Due to the limited
364 number of experimental data, as well as the value of R^2 equal to 0.65, equation (15) can be used
365 here for model verification at laboratory scale but should be used with extreme care (if at all) to
366 predict bedform characteristics in other experimental facilities or at field scales.

367 The active layer thickness, L_a , is set equal to $n_\sigma\sigma$ to capture the reduction in active layer
368 thickness in equilibrium bedrock reaches [Jafarinik *et al.*, 2019]. In the simulations presented
369 below $n_\sigma = 1$. If the probability density function of bed elevations is approximated with a
370 Gaussian distribution [Singh *et al.*, 2011], ~ 68% of the changes in bed elevation are contained in
371 an interval of amplitude σ around the mean bed level [Jafarinik *et al.*, 2019].

372

373 3.3 Calculation of the flow resistances

374 The experiments presented in Jafarinik *et al.*, [2019] were performed in a 0.19 m wide
375 laboratory flume, thus for a proper calculation of the flow resistances and of the shear stresses
376 acting on the channel bed, the different roughness between the rough bed and the smooth flume
377 sidewalls must be accounted for [Vanoni and Brooks, 1957]. Hence, we implemented the
378 Vanoni and Brooks [1957] sidewall correction procedure as described in Chiew and Parker
379 [1994] to estimate flow resistances and bed shear stress from laboratory data collected in narrow
380 flumes. It suffices to say here that to compute the flow resistances associated with the presence

381 of a granular bed in a narrow flume with smooth sidewalls, the cross section has to be divided in
 382 two regions, the bed region, where the flow is primarily impacted by the presence of the rough
 383 bed, and the wall region where flow characteristics are primarily controlled by the smooth
 384 sidewalls [see *Viparelli et al.*, 2014 for details on the implementation].

385 Here we use the subscript b to refer to sidewall corrected values, i.e. values
 386 characteristics of the granular bed. Equation (7) can thus be rewritten as

$$C_{fb}^{-1/2} = \alpha_r \left(\frac{R_{h,b}}{k_c} \right)^{\frac{1}{6}} \quad (16)$$

387 where $R_{h,b}$ is the hydraulic radius in the bed region [*Chiew and Parker*, 1994] and k_c is a cross-
 388 sectionally averaged composite roughness height that accounts for 3 different types of flow
 389 resistances, 1) flow resistances associated with the presence of a granular bed (skin friction), 2)
 390 flow resistances associated with the presence of bedforms (form drag) and 3) flow resistances
 391 associated with irregularities of the bedrock surface.

392 To implement equation (16) in the morphodynamic model presented above, we need a
 393 predictive formula for k_c . Here, due to the lack of experimental data on bedform geometry in
 394 bedrock reaches, we use an exponential regression on the experimental data by *Jafarinik et al.*
 395 [2019] presented in Figure 5.

$$\frac{k_c}{D_{s90}} = 0.17 e^{0.35 \frac{\sigma}{D_{sg}}} \quad (17)$$

396 where D_{s90} is the diameter of the bed surface sediment such that 90% of the sediment is finer and
 397 σ/D_{sg} is computed with equation (15). It is important to recognize that equation (17) is
 398 experiment-specific and should not be regarded as a general formulation applicable to other
 399 cases.

400 Form drag does not contribute to bedload transport [e.g. *Engelund and Hansen, 1967*],
 401 thus the cross-sectionally averaged bed shear stress associated with skin friction has to be
 402 computed for bedload transport calculation. We consider an ideal flow over a plane bed with the
 403 same energy gradient S_f and mean flow velocity U as the flow in presence of bedforms [see
 404 *Parker, 2004* for the case of alluvial beds]. The bed shear stress associated with skin friction is
 405 thus equal to $\rho C_{f,s} U^2$ with ρ being the water density and $C_{f,s}$ the skin friction coefficient. To
 406 compute $C_{f,s}$ with equation (7), the cross-sectionally averaged roughness height associated with
 407 skin friction $k_{s,c}$ has to be determined. In the formulation presented herein $k_{s,c}$ is equal to

$$k_{s,c} = p_c k_{s,a} + (1 - p_c) k_{s,b} \quad (18)$$

408 where $k_{s,a}$ and $k_{s,b}$ are the roughness heights associated with skin friction for the alluvium and
 409 for the bedrock respectively. In the model simulations presented below $k_{s,a}$ is assumed to be
 410 $2D_{s90}$ and $k_{s,b}$ is equal to the roughness height of the model bedrock in *Jafarinik et al. [2019]*
 411 experiment i.e. 0.1 mm. Equation (7) is thus rewritten as

$$C_{f,s}^{-1/2} = \alpha_r \left(\frac{R_{h,s}}{k_{s,c}} \right)^{1/6} \quad (19)$$

412 where $R_{h,s}$ is the hydraulic radius of the ideal flow. Unknowns in equation (19) are $C_{f,s}$ and $R_{h,s}$,
 413 thus a second equation is needed to solve the problem. The condition of equal friction slope for
 414 the real and the ideal flows is expressed with the aid of equation (6) as

$$\frac{C_f}{R_h} = \frac{C_{f,s}}{R_{h,s}} \quad (20)$$

415 Equations (19) and (20) are iteratively solved to determine $C_{f,s}$ and $R_{h,s}$.

416

417 *3.4 Bedload transport formulation*

418 The Ashida and Michiue bedload transport relation is used for model verification because
 419 it reasonably reproduces total and grain size specific sediment fluxes in the experiments with
 420 exposed bedrock [Jafarinik *et al.*, 2019]. When the non-uniformity of the bed material grain size
 421 is accounted for in models of river morphodynamics, the grain size distribution of the bed
 422 material is described in terms of M characteristic grain size diameters D_i . The Ashida and
 423 Michiue bedload relation for mixtures of sediment particles differing in size takes the form
 424 [Parker, 2008]

$$425 \quad q_{bi}^* = 17(\tau_{bsi}^* - \tau_{refi}^*) \left(\sqrt{\tau_{bsi}^*} - \sqrt{\tau_{refi}^*} \right) \quad (21)$$

426 where q_{bi}^* is the grain size specific Einstein number, i.e. the non-dimensional volumetric bed
 427 material load per unit channel width; τ_{bsi}^* denotes the grain size specific Shields number
 428 associated with skin friction, i.e. the non-dimensional bed shear stress associated with skin
 429 friction; and τ_{refi}^* is the grain size specific reference Shields number for the initiation of
 430 significant bedload transport of particles with characteristic grain size D_i [Parker, 2008]. The
 431 grain size specific Einstein number and the grain size specific Shields number associated with
 432 skin friction are respectively defined in equations (22) and (23) as

$$q_{bi}^* = \frac{q_{bi}}{\sqrt{RgD_i}D_i p_c F_i} \quad (22)$$

$$\tau_{bsi}^* = \frac{\tau_{bs}}{\rho RgD_i} \quad (23)$$

433 where R denotes submerged specific gravity of the sediment and τ_{bs} is the bed shear stress
 434 associated with skin friction.

435 The grain size specific reference value of the Shields number of equation (21) is
 436 computed with the hiding/exposure function [Parker, 2008]

$$\frac{\tau_{refi}^*}{\tau_{srg}^*} = \begin{cases} 0.843 \left(\frac{D_i}{D_{sg}} \right)^{-1} & \text{for } \frac{D_i}{D_{sg}} \leq 0.4 \\ \left[\frac{\log(19)}{\log(19 \frac{D_i}{D_{sg}})} \right]^2 & \text{for } \frac{D_i}{D_{sg}} > 0.4 \end{cases} \quad (24)$$

437 where τ_{srg}^* is a reference value equal to 0.05 [Parker, 2008].

438

439 **4 Model validation**

440 Model validation is performed in two phases, we first compare model results and alluvial
 441 equilibrium experiments to verify that the present formulation is able to reproduce the
 442 equilibrium characteristics of a fully alluvial system. We then compare experimental
 443 measurements and numerical predictions of equilibrium conditions in the experiments with
 444 bedrock reaches. Model boundary conditions for the validation runs are summarized in Table 1
 445 in terms of flow rate, sediment feed rate, sediment type (uniform or non-uniform sand of Figure
 446 2), downstream water surface base level (ξ_d), alluvial equilibrium water depth (H_o) and the reach
 447 type, i.e., alluvial or with exposed bedrock.

448

449 *4.1 Alluvial equilibrium runs*

450 The comparison between measured and modeled alluvial equilibrium water depth, bed
 451 slope, bed shear stress associated with skin friction and the geometric mean diameter of the
 452 surface material are respectively presented in Figure 6 panels a-d. In the plots of Figure 6 the
 453 numerical equilibrium values are on the horizontal axes and the measured values are on the

454 vertical axes. The continuous black lines denote perfect agreement between numerical
455 predictions and experimental observations. Each black diamond represents an alluvial
456 equilibrium experiment (odd runs in Table 1). Dashed grey lines represent error bounds around
457 the line of perfect agreement. Numerical predictions of water depth and flow velocity are within
458 20% error from the experimental observations. Numerical predictions of bed slopes are within
459 30% error of the measured value. The comparison between numerical and experimental
460 predictions of shear stresses associated with skin friction and geometric mean diameter of the
461 surface material are also within 30% and 10% error respectively. Therefore, Figure 6 shows that,
462 given the model simplifications and the use of empirical relations to compute the flow
463 resistances and the sediment fluxes, the proposed model is able to capture the experimental
464 observations with errors that are comparable with those of other one-dimensional, active layer-
465 based models of alluvial morphodynamics that account for the non-uniformity of the bed
466 material [e.g. *Viparelli et al.*, 2010; *Viparelli et al.*, 2014].

467

468 *4.2 Equilibrium runs with a bedrock reach*

469 The comparison between numerical predictions and experimental measurements is
470 presented in Figure 7 in terms of water surface and bed elevations (panels a, c, f and i), alluvial
471 cover (panels b, d, g, and j), and geometric mean diameter of the bed surface sediment (panels e,
472 h and k). Results for the run with uniform sand, i.e., Run 2, are presented in panels a and b.
473 Results for the runs with non-uniform bed material are in panels c-k. In particular, the
474 comparison for Run 4 is in panels c-e, the comparison for Run 6 is in panels f-h, and the
475 comparison for Run 8 is in panels i-k. Vertical dashed blue lines identify the position of the
476 alluvial-bedrock transition. In panels a, c, f and i, black diamonds and grey triangles are

477 respectively experimental water and bed surface elevations, grey and black lines respectively
478 represent the numerical water and bed surface elevations. In panels b, d, g and j, black diamonds
479 and grey lines are respectively experimental and numerical values of alluvial cover. In panels e,
480 h and k, black diamonds and grey lines represent experimental and numerical geometric mean
481 diameter of the bed surface material. Error bars in Figure 7 (panels a, c, f and i) denote 10%
482 error for the water surface elevation and 20% error for bed elevation. Modeled equilibrium bed
483 and water surface elevations are mostly within the error bars and thus in reasonable agreement
484 with the experimental results in the bedrock reaches.

485 The alluvial cover is equal to one in alluvial reaches, i.e. where the bed is entirely
486 covered with sediment, and it is less than one in the bedrock reaches, where the channel bed is
487 partially covered with sediment. Alluvial cover plots (panels b, d, g and j) show that the model
488 is able to reasonably capture the position of the alluvial-bedrock transition. However, the sudden
489 drop in alluvial cover measured in the experiments downstream of the alluvial-bedrock transition
490 is not reproduced in the numerical results. The model only captures measured rates of alluvial
491 cover reduction in the streamwise direction, as shown in Figure 7 with the slopes of regression
492 lines through the numerical results (grey line) and through the experimental points (green dash
493 line). In other words, the grey and the black lines in panels b, d, g and j are nearly parallel
494 showing similar rates of change in alluvial cover in the streamwise direction in the experimental
495 and in the numerical results. The difference between numerical predictions and the experimental
496 results is associated with small-scale phenomena associated with complex flow characteristics
497 that cannot be captured with the proposed formulation. Some of the small-scale phenomena are
498 illustrated in the Supplementary Video showing how flow separation downstream of a bedform,

499 as well as bedload transport on the model bedrock surface, cause a rapid increase in the fraction
500 of exposed bedrock.

501 The comparison between predicted and measured geometric mean diameters of the
502 equilibrium bed surface sediment are presented in panels e, h and k. Black diamonds represent
503 experimental points and continuous lines are model predictions. Error bars indicate 5% error and
504 most of the points fall within these bars (except 2 points in run 6 and 2 points in run 8)
505 suggesting a remarkably good agreement between numerical and predicted grain size
506 distributions of the bed surface sediment.

507 The comparison between numerical and measured grain size distribution (GSD) of the
508 surface material is presented in Figure 8 for samples collected at 0.81 m, 2.81 m and 4.81 m from
509 the test reach entrance. In this figure, black diamonds denote experimental measurements, lines
510 are the model prediction, and error bars indicate 10% variability around the measured data.
511 Results for Run 4 (flow rate of 20 l/s and feed rate of 700 gr/min) are panels a-c. Panels d-f
512 present the comparison between numerical and experimental results for Run 6 (flow rate of 20 l/s
513 and feed rate of 400 gr/min); and the numerical and experimental results for Run 8 (flow rate of
514 10/s and feed rate of 400 gr/min) are in panels g-i. Figure 8 confirms that the proposed model is
515 able to predict the grain size distribution of the equilibrium bed surface (and thus the bed
516 material fluxes) with errors that are comparable with (if not smaller than) those of one-
517 dimensional models of alluvial morphodynamics [e.g. *Viparelli et al., 2010; Viparelli et al.,*
518 *2014*].

519

520 **5 Discussion**

521 The validated model is used herein to investigate 1) spatial changes in equilibrium grains size
522 distribution of the bed surface sediment, flow characteristics and alluvial cover fraction when the
523 bedrock surface slope S_b is steeper than the alluvial equilibrium slope S_o in presence of a stable
524 bedrock-alluvial transition [Viparelli et al., 2015]; 2) spatial and temporal changes in the position
525 of a stable alluvial-bedrock transition in response to rising/falling downstream water surface base
526 level; and 3) whether or not the model is able to capture runaway alluviation and initial-condition
527 dependent equilibrium observed in experiments with steep bedrock surfaces by *Chatanantavet*
528 *and Parker* [2008].

529

530 *5.1 mixed bedrock-alluvial reach upstream of a bedrock-alluvial transition*

531 A stable bedrock-alluvial transition, i.e., a transition from a bedrock to an alluvial reach,
532 may form when the slope of the bedrock surface S_b is larger than the alluvial equilibrium slope S_o
533 of a river reach subject to the same flow regime and sediment supply. In particular, an
534 equilibrium bedrock-alluvial transition forms when the vertical distance between the downstream
535 bedrock surface and the water level V_d is small enough so that water depth H upstream of the
536 transition is smaller than the sum of the alluvial equilibrium water depth H_o and the minimum
537 thickness of alluvial cover L_{ac} . This is schematically represented in Figure 9 where the black line
538 shows the bedrock surface, the grey line denotes the elevation of the alluvium, the blue line
539 represents the water surface elevation and the dashed grey line represents the minimum thickness
540 for complete alluviation.

541 In these simulations we use the same flume geometry of the model validation runs;
542 bedrock surface slope $S_b = 0.005$; bed material, flow rate and feed rate of Run 4, i.e., non-
543 uniform sand, feed rate equal to 700 gr/min and flow rate equal to 20 l/s; downstream water

544 surface base level $\xi_d = 0.17$ m corresponding to $V_d = 0.17$ m, because the datum is located on the
545 model bedrock surface. The minimum thickness of alluvial cover, active layer thickness and
546 flow resistances calculation procedures are the same as those of the model validation runs.

547 Equilibrium results are presented in Figure 10 where panel a shows equilibrium elevation
548 of the alluvial bed surface (orange line) and of the bedrock (black line). The dashed grey line
549 identifies the minimum thickness of alluvial cover for complete alluviation of the channel bed,
550 the red circle and the dashed green line identify the equilibrium position of the bedrock-alluvial
551 transition. Spatial changes in equilibrium water depth are presented in Figure 10b where the blue
552 line denotes the water depth and the dashed green line identifies the position of the bedrock-
553 alluvial transition. In the bedrock reach upstream of the bedrock-alluvial transition the flow
554 depth increases in the flow direction until it reaches the alluvial equilibrium value H_o at the
555 bedrock-alluvial transition. The water depth remains constant in space and equal to H_o over the
556 alluvial reach.

557 The spatial increase in flow depth presented in Figure 10b is associated with a streamwise
558 decrease in mean flow velocity and bedload transport capacity of the flow. Recalling that at
559 equilibrium the bedload transport rate is equal to the sediment supply, a spatial decrease in
560 bedload transport capacity must be associated with an increase in alluvial cover p_c , equation (22).
561 The predicted streamwise increase of alluvial cover in the bedrock reach is presented in Figure
562 10c, where the dashed green line identifies the location of the bedrock-alluvial transition. In the
563 alluvial reach $p_c = 1$ and the bedload transport rate is everywhere equal to the bedload transport
564 capacity of the flow and to the sediment supply.

565 The spatial variation of equilibrium geometric mean diameter of bed surface sediment D_{sg}
566 is presented in Figure 10d. In the alluvial reach D_{sg} does not vary in space. In the bedrock reach,

567 it increases in the flow direction until it reaches its alluvial equilibrium value at the bedrock-
568 alluvial transition. The downstream coarsening of the bed surface sediment in the bedrock reach
569 can be explained considering that, due to the spatial deceleration of the flow, the bed material
570 transport capacity decreases in the flow direction. Consequently, the mobility of coarse grains
571 decreases more than the mobility of fine grains, and the volume fraction content of coarse
572 sediment in the bed surface sediment has to increase to ensure that sediment mass is conserved.

573 The numerical results of Figure 10 show that when the slope of the bedrock surface is
574 steeper than the alluvial equilibrium slope of a fluvial reach subject to the same flow and
575 sediment supply, flow characteristics of the bedrock reach tend to be characterized by spatial
576 flow deceleration associated with streamwise increase in alluvial cover and formation of a
577 pattern of downstream coarsening of the bed surface sediment. Conversely, when the slope of
578 the bedrock surface is milder than the alluvial equilibrium slope of a river reach subject to the
579 same flow regime and sediment supply (experiments of *Jafarinik et al.* [2019]), the flow
580 hydrodynamics in the bedrock reach is characterized by flow acceleration in the streamwise
581 direction associated with a reduction of alluvial cover and the formation of a pattern of
582 downstream fining of the bed surface sediment.

583 Due to the lack of predictive models of bedform regime and bedform size in bedrock
584 reaches, spatial changes in bedform geometry have not been predicted. We hypothesize that
585 lower regime bedform height may increase in the streamwise direction upstream of a stable
586 bedrock-alluvial transition. The experiments by *Jafarinik et al.* [2019] suggested that in the case
587 of spatial flow acceleration the bedform regime tend to move from dunes to antidunes with a
588 reduction of the flow resistances associated with form drag. In the case of the spatial flow
589 deceleration observed upstream of a stable bedrock-alluvial transition, we expect to see an

590 increase in dune height associated with an increase in flow depth, reduction in mean flow
591 velocity and increasing flow resistances associated with form drag.

592

593 *5.2 Impacts of sea level rise/fall on alluvial-bedrock transitions*

594 In low-slope bedrock rivers, equilibrium characteristics may be affected by changes in
595 sea level, i.e. the downstream water surface base level ξ_d . Here we use our validated model to
596 study the effects of sea level rise on flow characteristics and sediment transport processes in a
597 mixed bedrock reach characterized by an alluvial-bedrock transition.

598 Input parameters are the sediment size distribution, flow rate and feed rate of Run 4, i.e.
599 20 l/s of flow rate and 700 gr/min of feed rate. We widen the flume from 0.19 m to 1 m to avoid
600 using complicated procedures to remove side wall effects, we elongate the test reach to 30 m and
601 made the bedrock slope steep enough (~ 0.0015) to clearly show the movement of the alluvial-
602 bedrock transition along the reach. In these conditions, the alluvial equilibrium slope S_o is 0.002.
603 Simulations with increasing sea level start with an equilibrium bed. The downstream water
604 surface elevation is then raised in four, 3 mm increments for a total raise of 12 mm. After each
605 increase of downstream water surface elevation, the model is run until new equilibrium
606 conditions are obtained. After each sudden raise in downstream water level, the alluvial-bedrock
607 transition starts to move downstream until it stabilizes.

608 Figure 11 shows the equilibrium elevation of the alluvium for different values of
609 downstream water surface level, the bedrock surface (continuous brown line) and how the stable
610 alluvial-bedrock transition moves downstream following each increase in downstream water
611 surface level. Panels a, b, c in Figure 12 respectively show equilibrium alluvial cover, geometric
612 mean diameter of the surface material (D_{sg}) and water depth. At each location equilibrium water

613 depth, alluvial cover and D_{sg} increase in response to an increase in the water base level. In Figure
614 12, the location where the horizontal lines meet the inclined lines are the alluvial-bedrock
615 transition that moves downstream with base level rise.

616 These results confirm that the alluvial-bedrock transition can move upstream or
617 downstream when sea level rise, subsidence or uplift are present [Viparelli *et al.*, 2015]. We thus
618 expect that in response to base level fall the stable position of an alluvial-bedrock transition will
619 migrate upstream, and at each location of the initial bedrock reach the average fraction of
620 exposed bedrock will increase, the bed surface sediment will become finer and the water depth
621 will be shallower. Similarly, the stable position of a bedrock-alluvial transition in presence of
622 sea level rise is expected to migrate upstream, and at a given location in the initial bedrock reach
623 the alluvial cover will increase in time, the bed surface sediment will coarsen, and the water
624 depth will deepen. In response to base level fall, a stable bedrock-alluvial transition is expected
625 to migrate downstream with consequent reductions of water depth and alluvial cover in the
626 bedrock reach associated with fining of the bed surface sediment.

627

628 5.3 Application to steep bedrock reaches

629 *Chatanantavet and Parker* [2008] performed experiments with bedrock roughness height
630 of the bedrock surface smaller than the grain roughness of the alluvial patches, i.e., the same
631 condition of the *Jafarinik et al.* [2019] experiments used for model validation. In experiments
632 with bedrock slopes steeper than ~ 0.005 that commenced with a bare bedrock surface, alluviation
633 of the channel bed was not observed until the sediment feed rate exceeded a threshold value, then
634 rapid deposition of sediment on the channel bed was observed. *Chatanantavet and Parker*
635 [2008] called this rapid deposition of sediment *runaway alluviation*. Further, for bedrock slopes

636 steeper than ~ 0.015 *Chatanantavet and Parker* [2008] found that equilibrium was dependent on
637 the initial thickness of alluvium. When the initial thickness of alluvium was smaller than a
638 threshold value, the initial alluvial cover was washed out and equilibrium corresponded to a
639 condition of bare bedrock. If the initial thickness of alluvium was larger than the threshold
640 value, equilibrium conditions with $p_c < 1$ were obtained.

641 To test the model formulation presented herein on steep bedrock slopes, we tried to
642 model runaway alluviation and initial condition dependent equilibrium. We modified the model
643 to simulate the *Chatanantavet and Parker* [2008] experimental conditions of interest. We
644 considered uniform sediment and we substituted the quasi-steady approximation with a quasi-
645 normal approximation to easily model the *Chatanantavet and Parker* [2008] supercritical flows,
646 i.e. the water depth at each computational node was computed with a Chezy formulation [*Parker*
647 *et al.*, 2004].

648 Model results show that the model formulation presented herein is inadequate to
649 reproduce runaway alluviation and the initial-condition dependent equilibrium. We hypothesize
650 that the reason of model failure is in the flow model, which does not track the position of each
651 alluvial and bedrock area. It uses a cross-sectionally averaged roughness height to compute flow
652 resistance and bed shear stresses. This formulation cannot capture the effects of changes in
653 roughness height from alluvial to bedrock patches (and vice versa) on bedload transport. In
654 paragraph 11, *Chatanantavet and Parker* [2008] note that *bare bedrock surfaces were able to*
655 *accommodate much higher bedload transport rates without alluviation*. A similar sudden
656 change in bedload transport capacity was observed by *Jafarink et al.* [2019] in front of the lee
657 faces of the downstream migrating bedforms, as shown in the Supplementary Video and

658 discussed above to explain the differences between numerical and experimental cover fractions
659 in Figure 7.

660

661 **6 Conclusions**

662 We present a novel formulation for the alluvial morphodynamics of bedrock rivers that
663 explicitly accounts for the non-uniformity of the sediment size and for the different roughness
664 between the exposed bedrock and the alluvial patches. Flow resistances are further partitioned
665 between skin friction and form drag to properly account for the presence of small scale bedforms
666 in the sediment transport calculations.

667 This formulation, implemented in a numerical model, is validated against the
668 experimental results by *Jafarinik et al.* [2019]. The differences between the numerical
669 predictions and the experimental observations in the bedrock reaches are comparable with the
670 differences between numerical and experimental values presented in similar studies on the
671 alluvial morphodynamics of fluvial reaches. Model validation is performed for an equilibrium
672 bedrock reach downstream of an alluvial-bedrock transition, which is characterized by spatial
673 flow acceleration on the bedrock reach associated with a streamwise decrease in the alluvial
674 cover, fining of the bed surface sediment and reduction of bedform height.

675 Model application to study the alluvial morphodynamics of bedrock reaches upstream of
676 a stable bedrock-alluvial transition reveals that the equilibrium flow on the bedrock reach is
677 characterized by flow deceleration in the downstream direction. This flow deceleration is
678 associated with a streamwise increase of the alluvial cover and the formation of a stable pattern
679 of downstream coarsening of the bed surface sediment to balance the reduction of the bedload

680 transport capacity. Based on experimental observations, we hypothesize that if dunes form on
681 the alluvial reach, the bedform height in the bedrock reach should increase in the flow direction.

682 The validated model is also used to study the effects of water surface base level rise/fall
683 on the characteristics and sediment transport processes on low-slope bedrock reaches
684 characterized by an alluvial-bedrock or a bedrock-alluvial transition. The results show that
685 notwithstanding these transitions are stable features of bedrock reaches in equilibrium, their
686 locations can move upstream or downstream in response to changes in water surface base level.

687 Finally, the model is tested to reproduce runaway alluviation and initial condition
688 dependent equilibrium in steep bedrock reaches [*Chatanantavet and Parker, 2008*], which are
689 due to the differences between bedload transport capacity on the bedrock surface and on the
690 alluvial surface. In the flow model used herein the roughness height used to compute flow
691 resistance and bed shear stress is a cross sectionally average value. The model is thus incapable
692 of reproducing phenomena associated with the different roughness between bedrock and alluvial
693 patches the bedrock and alluvium such as runaway alluviation and initial condition dependent
694 equilibrium.

695

696

697 **Acknowledgements**

698 This research was supported by the United States National Science Foundation through award
699 EAR 1250641 and by the University of South Carolina. The model (code transcript in Fortran
700 95) with proper documentation will soon (i.e. in the second half of February 2020) be made
701 publicly available through the model repository of the Community Surface Dynamics Modeling
702 System (CSDMS).

703

704

705

706

707

708

NOTATION

709	C_f	Friction coefficient
710	$C_{f,bs}$	Friction coefficient associated with skin friction
711	C_{fb}	Bed friction coefficient
712	D_g	Geometric mean diameter of the sediment supply
713	D_i	Grain size diameter
714	D_{90}	Grain size such that 90 percent of material are finer
715	F_i	Volume fraction content of sediment in the generic grain size range in the bed surface
716	f_i	Volume fraction content of sediment in the generic grain sizes
717	f'_i	Volume fraction content of sediment in the generic grain size range in the substrate
718	f_i	Volume fraction content of sediment in the generic grain sizes at active-substrate
719		interface
720	$f_{load,i}$	Volume fraction content of sediment in the generic grain sizes in bedload
721	Fr	Froude number
722	g	Acceleration of gravity
723	H	Water depth
724	H_o	Equilibrium water depth
725	k_c	Composite roughness height
726	k_{sc}	Roughness height associated with skin friction
727	k_{sa}	Roughness height associated with skin friction for alluvium
728	k_{sb}	Roughness height associated with skin friction for bedrock
729	L_{ac}	Minimum thickness of alluvial cover
730	L_a	Active layer thickness in fully alluvial reach

731	L_a'	Active layer thickness in bedrock reach
732	$L_{a,av}$	Average active layer thickness
733	p_c	Alluvial cover
734	p_b	Probability of not having bedrock at elevation z
735	p_{bt}	Probability that a point at active-substrate interface is either in alluvium or water
736	q_{bi}^*	Nondimensional bedload transport rate per unit width for a generic grain size
737	q_{bi}	Bedload transport rate per unit width of the generic grain size
738	q_{bic}	Bedload transport capacity of the generic grain size
739	q_{bT}	Total (summed over all the grain sizes) bedload transport rate per unit width
740	q_{bTc}	Total (summed over all the grain sizes) sediment transport capacity
741	q_w	Flow discharge per unit channel width
742	R	Submerged specific gravity
743	R_h	Hydraulic radius
744	$R_{h,s}$	Hydraulic radius associated with skin friction
745	$R_{h,b}$	Hydraulic radius in the bed region
746	S	Bed slope
747	S_b	Bedrock slope
748	S_f	Friction slope
749	S_o	Equilibrium bed slope
750	U	Averaged flow velocity
751	η	Average elevation of alluvial deposit
752	η_b	Bedrock elevation
753	λ_p	Bed material porosity

754	ζ_d	Water level at the downstream boundary
755	ρ	Water density
756	σ_g	Geometric standard deviation of the sediment supply
757	τ_{bs}^*	Shields number associated with skin friction
758	τ_{bsi}^*	Shields number associated with skin friction of the generic grain size
759	τ_{refi}^*	Reference Shields number of the generic grain size
760	τ_{scg}^*	Reference value for Shields number
761	V_d	Distance between water level and bedrock surface at downstream
762		
763		
764		
765		
766		
767		

768 **References**

- 769 Anderson, A. G., Parker, G., & Wood, A. (1975). *The flow and stability characteristics of*
770 *alluvial river channels*. Project Report 161, University of Minnesota St. Anthony Falls
771 Laboratory.
- 772 Blom, A. (2008). Different approaches to handling vertical and streamwise sorting in modeling
773 river morphodynamics. *Water resources research*, 44(3).
- 774 Blom, A., Parker, G., Ribberink, J. S., & De Vriend, H. J. (2006). Vertical sorting and the
775 morphodynamics of bed-form-dominated rivers: An equilibrium sorting model. *Journal of*
776 *Geophysical Research: Earth Surface*, 111(F1). doi: 10.1029/2004JF000175
- 777 Blom, A., Viparelli, E., & Chavarrías, V. (2016). The graded alluvial river: Profile concavity and
778 downstream fining. *Geophysical Research Letters*, 43(12), 6285-6293. doi:
779 10.1002/2016GL068898
- 780 Chatanantavet, P., & Parker, G. (2008). Experimental study of bedrock channel alluviation under
781 varied sediment supply and hydraulic conditions. *Water Resources Research*, 44(12). doi:
782 10.1029/2007WR006581
- 783 Chatanantavet, P., Whipple, K. X., Adams, M. A., & Lamb, M. P. (2013). Experimental study on
784 coarse grain saltation dynamics in bedrock channels. *Journal of Geophysical Research:*
785 *Earth Surface*, 118(2), 1161-1176. doi: 10.1002/jgrf.20053
- 786 Chaudhry, M. H. (2007). *Open-channel flow*. Springer Science & Business Media.
- 787 Chiew, Y. M., & Parker, G. (1994). Incipient sediment motion on non-horizontal slopes. *Journal*
788 *of Hydraulic Research*, 32(5), 649-660.
- 789 De Vries, M. (1965). *Considerations about non-steady bed-load-transport in open channels*.
790 Publication 36, Delft Hydraulics Laboratory, Netherlands.

791 Engelund, F., & Hansen, E. (1967). *A monograph on sediment transport in alluvial streams*.
792 Technical University of Denmark Østervoldgade 10, Copenhagen K.

793 Gasparini, N. M., Whipple, K. X., & Bras, R. L. (2007). Predictions of steady state and transient
794 landscape morphology using sediment-flux-dependent river incision models. *Journal of*
795 *Geophysical Research: Earth Surface*,112(F3). doi: 10.1029/2006JF000567

796 Hodge, R. A., Hoey, T. B., & Sklar, L. S. (2011). Bed load transport in bedrock rivers: The role
797 of sediment cover in grain entrainment, translation, and deposition. *Journal of Geophysical*
798 *Research: Earth Surface*, 116(F4). doi: 10.1029/2011JF002032

799 Hodge, R., Hoey, T., Maniatis, G., & Leprêtre, E. (2016). Formation and erosion of sediment
800 cover in an experimental bedrock-alluvial channel. *Earth Surface Processes and Landforms*.
801 doi: 10.1002/esp.3924

802 Hoey, T. B., & Ferguson, R. (1994). Numerical simulation of downstream fining by selective
803 transport in gravel bed rivers: Model development and illustration. *Water resources research*,
804 30(7), 2251-2260.

805 Inoue, T., Izumi, N., Shimizu, Y., & Parker, G. (2014). Interaction among alluvial cover, bed
806 roughness, and incision rate in purely bedrock and alluvial-bedrock channel. *Journal of*
807 *Geophysical Research: Earth Surface*,119(10), 2123-2146. doi: 10.1002/2014JF003133

808 Jafarinik, S., Hernández Moreira, R., & Viparelli, E. (2019). Alluvial morphodynamics of
809 bedrock reaches transporting mixed-size sand. Laboratory experiments. *Journal of*
810 *Geophysical Research: Earth Surface* 124, <https://doi.org/10.1029/2019JF005058>

811 Johnson, J. P. (2014). A surface roughness model for predicting alluvial cover and bed load
812 transport rate in bedrock channels. *Journal of Geophysical Research: Earth Surface*, 119(10),
813 2147-2173. doi: 10.1002/ 2013JF003000.

814 Lague, D. (2010). Reduction of long-term bedrock incision efficiency by short-term alluvial
815 cover intermittency. *Journal of Geophysical Research: Earth Surface*, 115(F2). doi:
816 10.1029/2008JF001210

817 Lague, D. (2014). The stream power river incision model: evidence, theory and beyond. *Earth*
818 *Surface Processes and Landforms*, 39(1), 38-61. doi: 10.1002/esp.3462

819 Lamb, M. P., Dietrich, W. E., & Sklar, L. S. (2008). A model for fluvial bedrock incision by
820 impacting suspended and bed load sediment. *Journal of Geophysical Research: Earth*
821 *Surface*, 113(F3). doi: 10.1029/2007JF000915

822 Lanzoni, S., & Seminara, G. (2002). Long-term evolution and morphodynamic equilibrium of
823 tidal channels. *Journal of Geophysical Research: Oceans*, 107(C1), 1-1.

824 Lauer, J. W., Viparelli, E., & Piégay, H. (2016). Morphodynamics and sediment tracers in 1-D
825 (MAST-1D): 1-D sediment transport that includes exchange with an off-channel sediment
826 reservoir. *Advances in Water Resources*, 93, 135-149.

827 Nelson, P. A., & Seminara, G. (2012). A theoretical framework for the morphodynamics of
828 bedrock channels. *Geophysical Research Letters*, 39(6), doi: 10.1029/2011GL050806

829 Nittrouer, J. A., Mohrig, D., Allison, M. A., & Peyret, A. P. B. (2011). The lowermost
830 Mississippi River: a mixed bedrock-alluvial channel *Sedimentology*, 58(7), 1914-1934. doi:
831 10.1111/j.1365-3091.2011.01245.x

832 Parker, G. (1991a). Selective sorting and abrasion of river gravel. I: Theory. *Journal of*
833 *Hydraulic Engineering*, 117(2), 131-147. doi: 10.1061/(ASCE)0733-9429(1991)117:2(131)

834 Parker, G. (1991b). Selective sorting and abrasion of river gravel. II: Applications. *Journal of*
835 *Hydraulic Engineering*, 117(2), 150-171.

836 Parker, G. (2004). *1D sediment transport morphodynamics with applications to rivers and*
837 *turbidity currents*. E-book available at Gary Parker's Morphodynamics Web Page, last
838 update April, 13, 2006.

839 Parker, G. (2008). Transport of gravel and sediment mixtures. *Sedimentation engineering:*
840 *Processes, measurements, modeling, and practice, 110, 165-252. doi:*
841 *10.1061/9780784408148.ch03.*

842 Parker, G. and Klingeman, P.C. (1982), On why gravel bed streams are paved, *Water Resources*
843 *Research, 18 (5), 1409–1433, 1982.*

844 Parker, G., Paola, C., & Leclair, S. (2000). Probabilistic Exner sediment continuity equation for
845 mixtures with no active layer. *Journal of Hydraulic Engineering, 126(11), 818-826.*

846 Shaw, J. B., Mohrig, D., & Whitman, S. K. (2013). The morphology and evolution of channels
847 on the Wax Lake Delta, Louisiana, USA. *Journal of Geophysical Research: Earth Surface,*
848 *118(3), 1562-1584. doi: 10.1002/jgrf.20123.*

849 Shaw, J. B., & Mohrig, D. (2014). The importance of erosion in distributary channel network
850 growth, Wax Lake Delta, Louisiana, USA. *Geology, 42(1), 31-34.*

851 Sklar, L. S., & Dietrich, W. E. (2004). A mechanistic model for river incision into bedrock by
852 saltating bed load. *Water Resources Research, 40(6). doi: 10.1029/2003WR002496*

853 Tuijnder, A. P., Ribberink, J. S., & Hulscher, S. J. (2009). An experimental study into the
854 geometry of supply-limited dunes. *Sedimentology, 56(6), 1713-1727. doi: 10.1111/j.1365-*
855 *3091.2009.01054.x*

856 Turowski, J. M., Lague, D., & Hovius, N. (2007). Cover effect in bedrock abrasion: A new
857 derivation and its implications for the modeling of bedrock channel morphology. *Journal of*
858 *Geophysical Research: Earth Surface, 112(F4). doi: 10.1029/2006JF000697*

- 859 Vanoni, V. A., & Brooks, N. H. (1957). *Laboratory studies of the roughness and suspended load*
860 *of alluvial streams*. Sedimentation Laboratory California Institute of Technology, Pasadena,
861 California, Report No. E-68.
- 862 Viparelli, E., Sequeiros, O. E., Cantelli, A., Wilcock, P. R., & Parker, G. (2010). River
863 morphodynamics with creation/consumption of grain size stratigraphy 2: numerical model.
864 *Journal of Hydraulic Research*, 48(6), 727-741.
- 865 Viparelli, E., Gaeuman, D., Wilcock, P., & Parker, G. (2011). A model to predict the evolution
866 of a gravel bed river under an imposed cyclic hydrograph and its application to the Trinity
867 River. *Water Resources Research*, 47(2). doi: 10.1029/2010WR009164
- 868 Viparelli, E., Nittrouer, J. A., & Parker, G. (2015). Modeling flow and sediment transport
869 dynamics in the lowermost Mississippi River, Louisiana, USA, with an upstream alluvial-
870 bedrock transition and a downstream bedrock-alluvial transition: Implications for land
871 building using engineered diversions. *Journal of Geophysical Research: Earth Surface*,
872 120(3), 534-563. doi: 10.1002/2014JF003257.
- 873 Whipple, K. X. (2004). Bedrock rivers and the geomorphology of active orogens. *Annu. Rev.*
874 *Earth Planet. Sci.*, 32, 151-185. doi: 10.1146/annurev.earth.32.101802.120356
- 875 Whipple, K. X., & Tucker, G. E. (2002). Implications of sediment-flux-dependent river incision
876 models for landscape evolution. *Journal of Geophysical Research: Solid Earth*, 107(B2). doi:
877 10.1029/2000JB000044
- 878 Whipple, K. X., Hancock, G. S., & Anderson, R. S. (2000). River incision into bedrock:
879 Mechanics and relative efficacy of plucking, abrasion, and cavitation. *Geological Society of*
880 *America Bulletin*, 112(3), 490-503. doi: 10.1130/0016-7606(2000)112

881 Wilcock, P. R., & Crowe, J. C. (2003). Surface-based transport model for mixed-size sediment.
882 *Journal of Hydraulic Engineering*, 129(2), 120-128. doi: 10.1061/(ASCE)0733-
883 9429(2003)129:2(120)

884 Wong, M., Parker, G., DeVries, P., Brown, T. M., & Burges, S. J. (2007). Experiments on
885 dispersion of tracer stones under lower-regime plane-bed equilibrium bed load transport.
886 *Water Resources Research*,43(3). doi: 10.1029/2006WR005172

887 Zhang, L., Parker, G., Stark, C. P., Inoue, T., Viparelli, E., Fu, X., & Izumi, N. (2015). Macro-
888 roughness model of bedrock-alluvial river morphodynamics. *Earth Surface Dynamics*, 3,
889 113-138. doi:10.5194/esurf-3-113-2015

890

891

892

893

894

895 List of Tables

896 Table 1. Experimental conditions for the model validation runs [Jafarinik *et al.*, 2019]. ξ_d denotes
897 the downstream water surface base level and H_o the alluvial equilibrium flow depth

898

899 List of Figures

900 Figure 1. Schematic geometry of the modeled domain. Black solid line is the bedrock surface.
901 Grey line is the bed surface and blue thick line represents the water surface. The red circle shows
902 the alluvial-bedrock transition. The dashed grey line denotes the active layer (L_a) thickness and
903 the dashed black line represents the minimum thickness of alluvial cover (L_{ac}).

904 Figure 2. Grain size distribution of the bedload material. Grey dashed line shows the GSD of
905 uniform material used in Run 1 and Run 2. Black solid line represents the GSD of non-uniform
906 material used in Runs 3-8.

907 Figure 3. Alluvial cover formulation of *Viparelli et al.* [2015] vs experimental data. Grey
908 diamonds are experimental points, the black line is equation (17) and the dashed lines indicate
909 $\pm 25\%$ around the predicted value.

910 Figure 4. Flow resistance closures based on the experimental data. Dimensionless standard
911 deviation of bed elevation fluctuation against Froude number. Grey diamonds represent the
912 experimental points and the lines represent regression line.

913 Figure 5. Dimensionless composite roughness height against dimensionless standard deviation of
914 bed elevation fluctuation. Grey diamonds represent the experimental points and the lines
915 represent regression line.

916 Figure 6. Comparison of experimental and numerical results for the fully alluvial runs. a) Water
917 depth, b) bed slope, c) shear stress associated with skin friction, d) geometric mean diameter of

918 the surface material. The black lines represent the perfect agreement between experimental and
919 numerical results. The dashed lines depict the errors around the perfect match.

920 Figure 7. Experimental and numerical comparison of water (ζ) and bed surface (η) elevation,
921 alluvial cover and geometric mean diameter of the surface material in Runs 2, 4, 6 and 8. The
922 points are experimental data and the solid lines are the numerical results. The blue dashed line
923 represents the location of alluvial-bedrock transition and the green dashed line denote the linear
924 regression of the experimental alluvial cover on the bedrock reach.

925 Figure 8. Comparison between experimental and numerical grain size distributions of bed
926 surface material at 0.81 m (upstream), 2.81 m (middle) and 4.81 m (downstream) from the test
927 reach entrance. Grey lines represent numerical results and the diamonds denote the experimental
928 data. Vertical bars denote 10% error

929 Figure 9. Schematic plot of a bedrock reach upstream of the bedrock-alluvial transition.

930 Figure 10. Numerical results with a stable bedrock-alluvial transition. a) bed surface (orange
931 line), bedrock elevation (black line) and the minimum thickness of alluvial cover (dashed grey
932 line). Red circle indicates the bedrock-alluvial transition. b) water depth. c) alluvial cover. D) the
933 geometric mean diameter of the surface sediment. The green dashed lines represent the bedrock-
934 alluvial transition

935 Figure 11. Location of stable alluvial-bedrock transition for base level rise. Brown solid and
936 dashed lines represent the bedrock surface and the minimum thickness for fully alluviation
937 respectively. The dark blue, yellow, green, light blue and purple lines are bed surface elevations
938 after 0, 3, 6, 9 and 12 mm of base level rise.

939

940 Figure 12. (a) Equilibrium water depth, (b) Geometric mean diameter of surface material and (c)
941 the alluvial cover . Dark blue, yellow, green, light blue and purple respectively represent the
942 initial equilibrium bed and equilibrium results after 3 mm, 6 mm, 9 mm and 12 mm base level
943 rise.
944
945

946 Table 1. Experimental conditions for the model validation runs [Jafarinik et al., 2019]. ξ_d denotes
 947 the downstream water surface base level and H_o the alluvial equilibrium flow depth

Run	Flow Rate (L/s)	Feed Rate (gr/min)	ξ_d (m)	H_o (m)	Grain Size	Condition
1	20	700	0.224	0.176	Uniform	Fully alluvial
2	20	700	0.160		Uniform	Exposed bedrock
3	20	700	0.223	0.172	Nonuniform	Fully alluvial
4	20	700	0.154		Nonuniform	Exposed bedrock
5	20	400	0.225	0.186	Nonuniform	Fully alluvial
6	20	400	0.186		Nonuniform	Exposed bedrock
7	10	400	0.146	0.086	Nonuniform	Fully alluvial
8	10	400	0.083		Nonuniform	Exposed bedrock

948

949

950

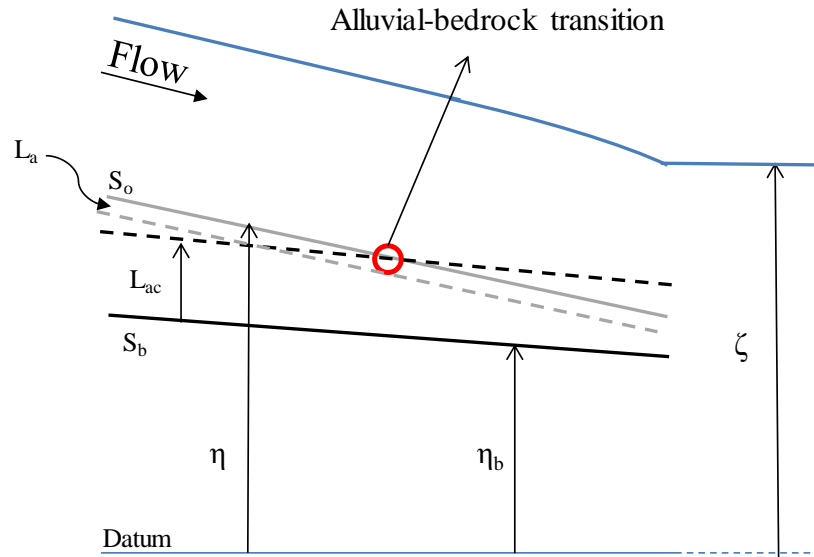
951

952

953

954

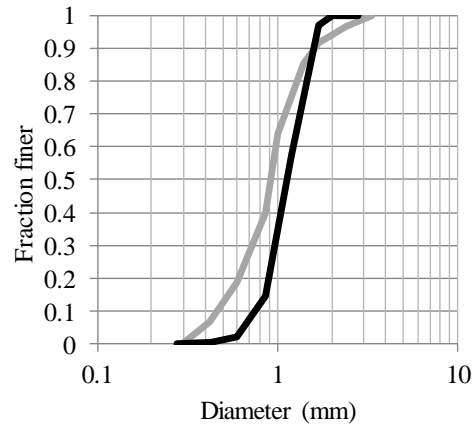
955



956

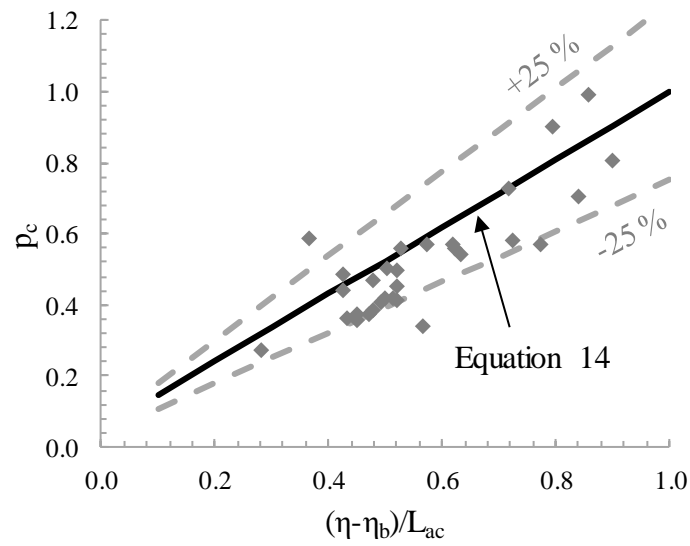
957 Figure 1. Schematic geometry of the model domain. Black solid line is the bedrock surface. Grey
 958 line is the bed surface and blue thick line represents the water surface. The red circle shows the
 959 alluvial-bedrock transition. The dashed grey line denotes the active layer (L_a) thickness and the
 960 dashed black line represents the minimum thickness of alluvial cover (L_{ac}).

961



962
 963 Figure 2. Grain size distribution of the bedload material. Grey dashed line shows the GSD of
 964 uniform material used in Run 1 and Run 2. Black solid line represents the GSD of non-uniform
 965 material used in Runs 3-8.

966
 967
 968

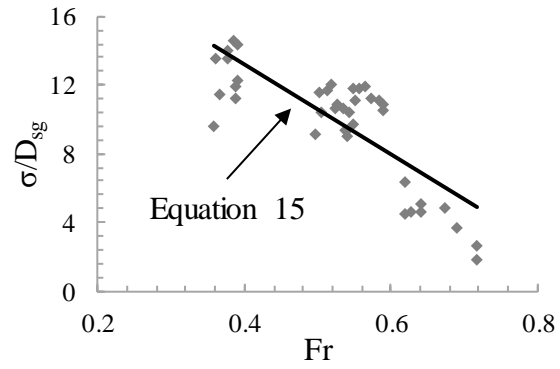


969
 970 Figure 3. Alluvial cover formulation of *Viparelli et al.* [2015] vs experimental data. Grey
 971 diamonds are experimental points, the black line is equation (17) and the dashed lines indicate
 972 $\pm 25\%$ around the predicted value.

973

974

975



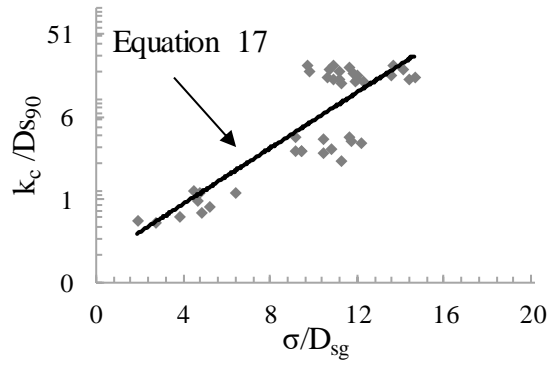
976
977

978

979 Figure 4. Flow resistance closures based on the experimental data. Dimensionless standard
980 deviation of bed elevation fluctuation against Froude number. Grey diamonds represent the
981 experimental points and the lines represent regression line.

982

983



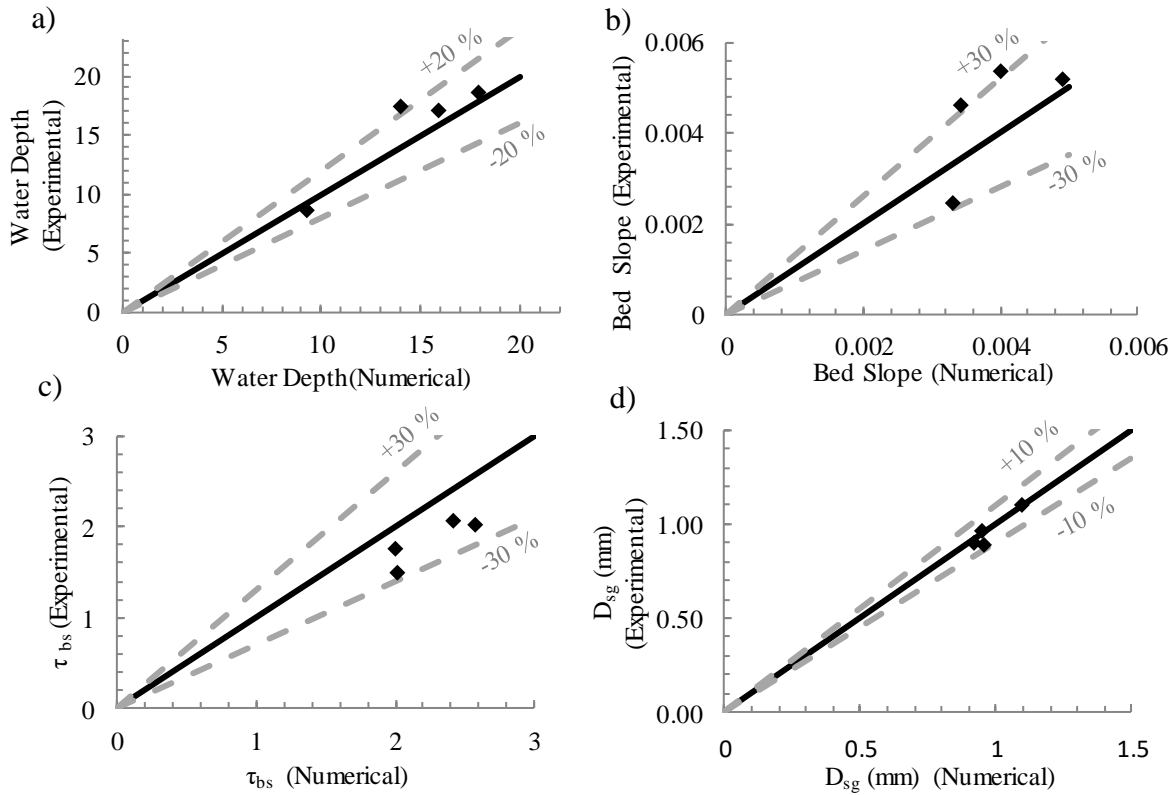
984

985 Figure 5. Dimensionless composite roughness height against dimensionless standard deviation of
986 bed elevation fluctuation. Grey diamonds represent the experimental points and the lines
987 represent regression line.

988

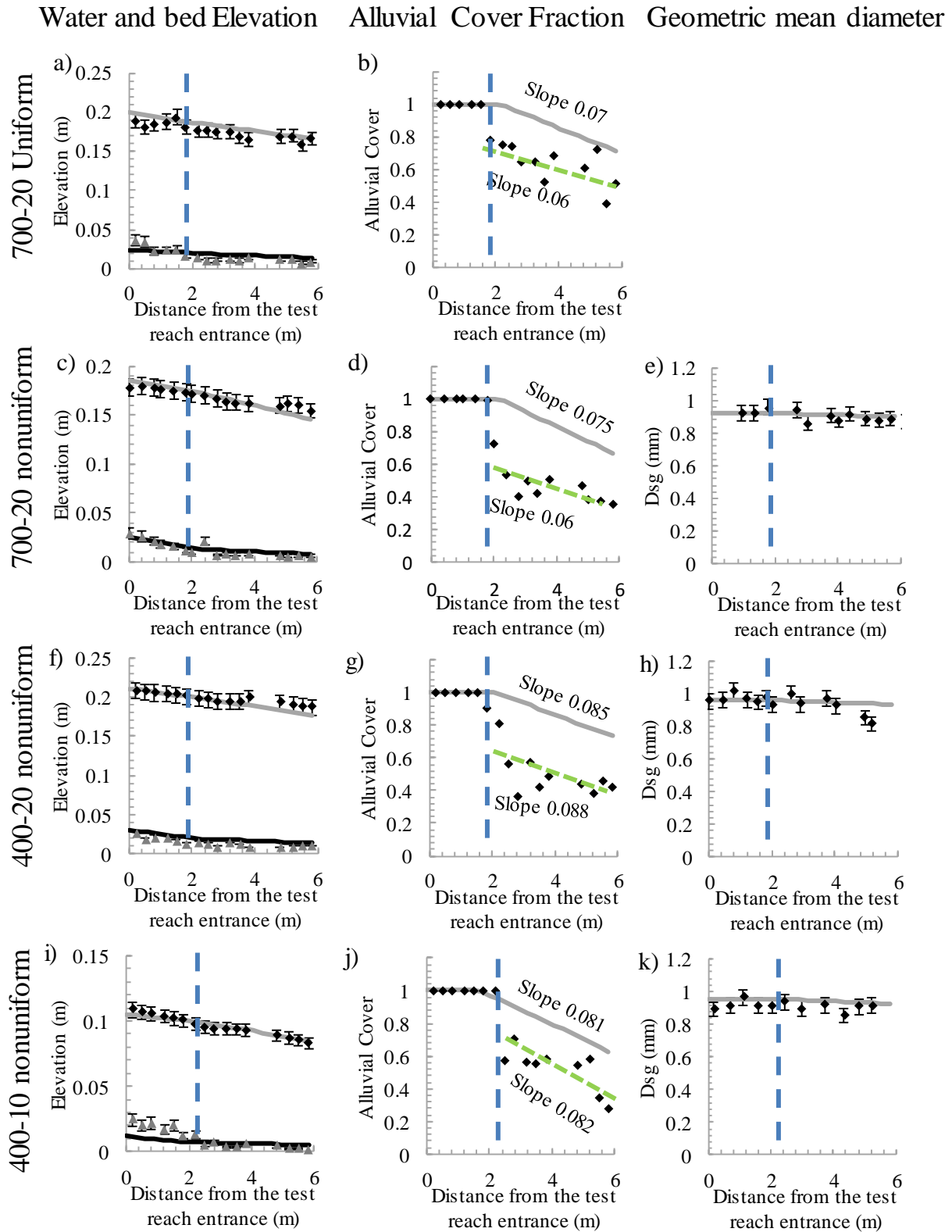
989

990



991
 992 Figure 6. Comparison of experimental and numerical results for the fully alluvial runs. a) Water
 993 depth, b) bed slope, c) shear stress associated with skin friction, d) geometric mean diameter of
 994 the surface material. The black lines represent the perfect agreement between experimental and
 995 numerical results. The dashed lines depict the errors around the perfect match.

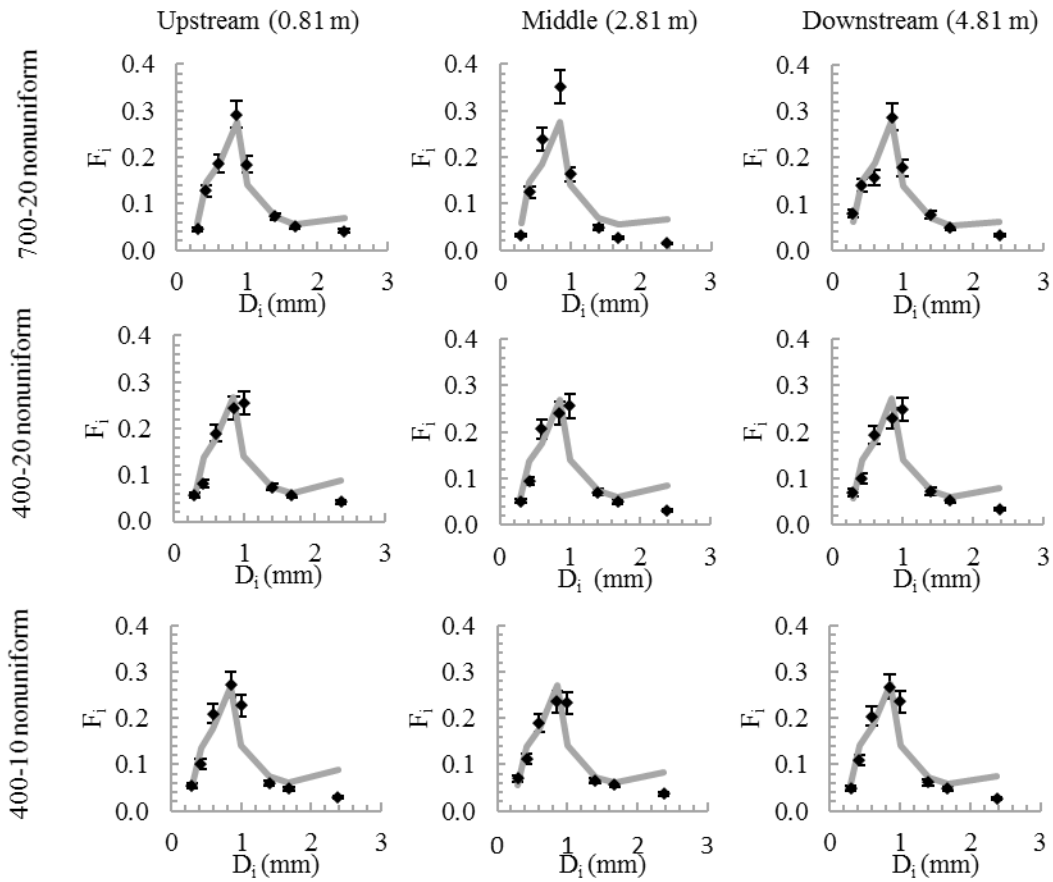
996



997
 998 Figure 7. Experimental and numerical comparison of water (ζ) and bed surface (η) elevation,
 999 alluvial cover and geometric mean diameter of the surface material in Runs 2, 4, 6 and 8. The

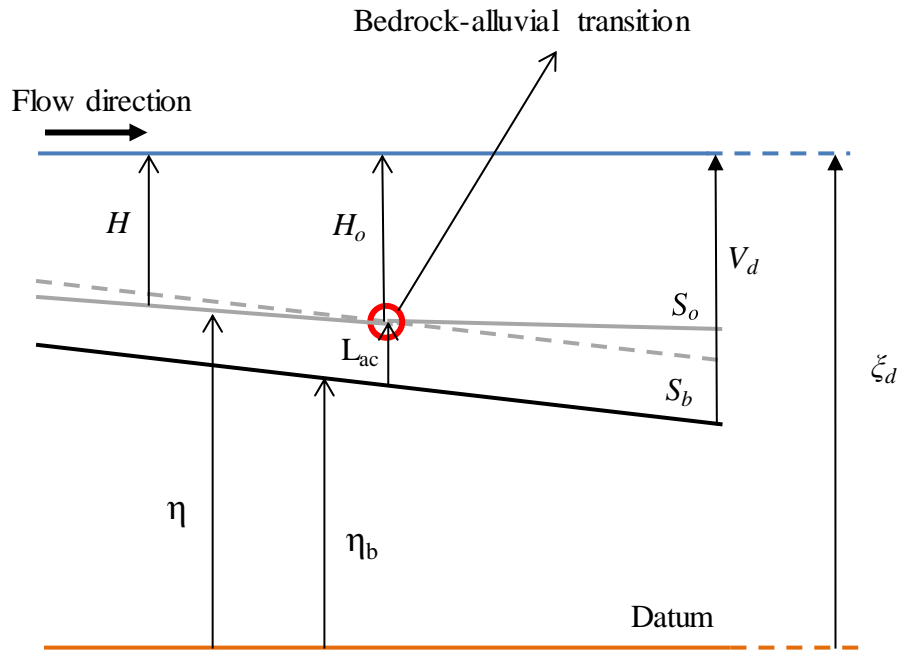
1000 points are experimental data and the solid lines are the numerical results. The blue dashed line
1001 represents the location of alluvial-bedrock transition and the green dashed line denote the linear
1002 regression of the experimental alluvial cover on the bedrock reach.

1003



1004
 1005 Figure 8. Comparison between experimental and numerical grain size distributions of bed
 1006 surface material at 0.81 m (upstream), 2.81 m (middle) and 4.81 m (downstream) from the test
 1007 reach entrance. Grey lines represent numerical results and the diamonds denote the experimental
 1008 data. Vertical bars denote 10% error.

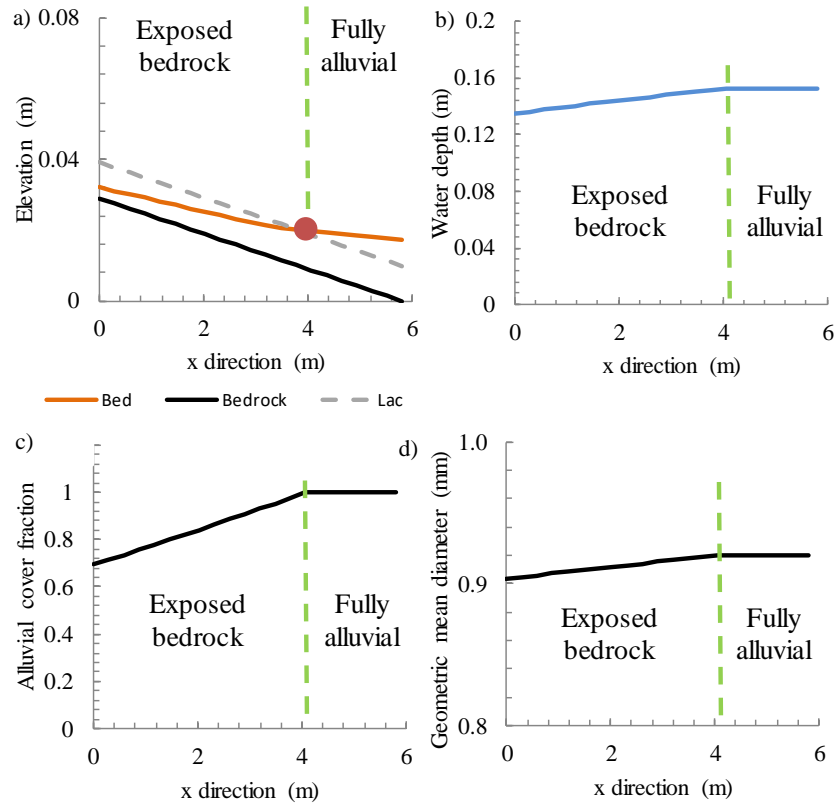
1009



1010

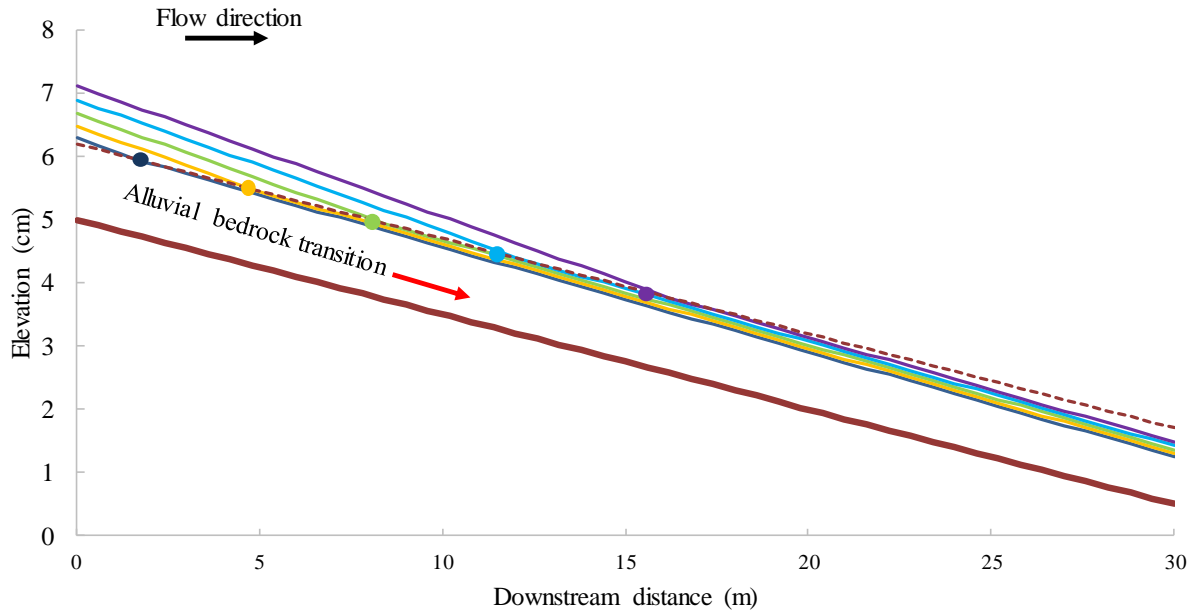
1011 Figure 9. Schematic plot of a bedrock reach upstream of a bedrock-alluvial transition.

1012



1013
 1014 Figure 10. Numerical results with a stable bedrock-alluvial transition. a) bed surface (orange
 1015 line), bedrock elevation (black line) and the minimum thickness of alluvial cover (dashed grey
 1016 line). Red circle indicates the bedrock-alluvial transition. b) water depth. c) alluvial cover. D) the
 1017 geometric mean diameter of the surface sediment. The green dashed lines represent the bedrock-
 1018 alluvial transition

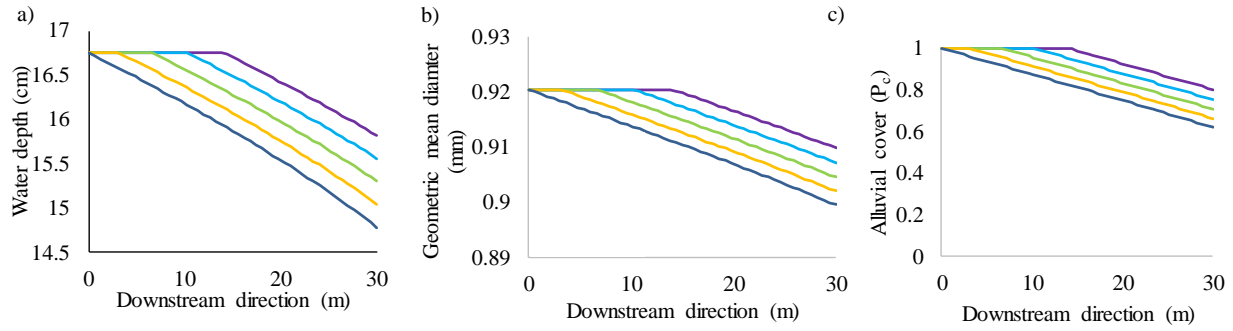
1019



1020
 1021 Figure 11. Location of stable alluvial-bedrock transition for base level rise. Brown solid and
 1022 dashed lines represent the bedrock surface and the minimum thickness for fully alluviation
 1023 respectively. Dark blue, yellow, green, light blue and purple respectively represent the initial
 1024 equilibrium bed and equilibrium results after 3 mm, 6 mm, 9 mm and 12 mm base level rise.

1025

1026



1027
 1028 Figure 12. (a) Equilibrium water depth, (b) Geometric mean diameter of surface material and (c)
 1029 the alluvial cover. Dark blue, yellow, green, light blue and purple respectively represent the
 1030 initial equilibrium bed and equilibrium results after 3 mm, 6 mm, 9 mm and 12 mm base level
 1031 rise.

1032
 1033